Dual-frequency sub-Doppler spectroscopy: extended theoretical model and microcell-based experiments

Denis Brazhnikov[1,2]*, Michael Petersen[3], Grégoire Coget[3], Nicolas Passilly[3],
Vincent Maurice[3,4], Christophe Gorecki[3], and Rodolphe Boudot[3,4]**
[1]*Institute of Laser Physics SB RAS, 15B Lavrentyev ave., 630090 Novosibirsk, Russia*
[2]*Novosibirsk State University, 2 Pirogov str., 630090 Novosibirsk, Russia*
[3]*FEMTO-ST, CNRS, UBFC, ENSMM, 26 rue de l'épitaphe, 25000 Besançon, France*
[4] *now at NIST, Time-Frequency Division, 325 Broadway, 80305 Boulder, Colorado, USA*
*brazhnikov@laser.nsc.ru, **rodolphe.boudot@femto-st.fr

Sub-Doppler spectroscopy in alkali vapor cells using two counter-propagating dual-frequency laser beams allows the detection of high-contrast sign-reversed natural-linewidth sub-Doppler resonances. However, to date, only a qualitative theory based on a simplified Λ-scheme model has been reported to explain underlying physics of this phenomenon. In this work, an extended theoretical model of dual-frequency sub-Doppler spectroscopy (DFSDS) for Cs D_1 line is reported. Taking into account the real atomic energy structure, main relaxation processes and various nonlinear effects, this model describes quantitatively the respective contributions of involved physical processes and predicts main properties (height and line-width) of the sub-Doppler resonances. Experimental tests are performed with a Cs vapor micro-fabricated cell and results are found to be in correct agreement with theoretical predictions. Spatial oscillations of the sub-Doppler resonance amplitude with translation of the reflection mirror are highlighted. A beat-note between two laser systems, including one stabilized with DFSDS on a Cs vapor microcell, yields a fractional frequency stability of $2\times10^{-12}\ \tau^{-1/2}$ until 10 s averaging time. These results demonstrate that DFSDS could be an interesting approach for the development of a high-performance microcell-based optical frequency reference, with applications in various compact quantum devices.

PACS: 42.62.Fi; 06.30.Ft
Keywords: *High-resolution laser spectroscopy, saturated-absorption resonances, quantum metrology, optical frequency stabilization, coherent population trapping, MEMS vapor cells, external-cavity diode lasers*

I. INTRODUCTION

Sub-Doppler spectroscopy [1-4] in alkali vapor cells is an exquisite approach to perform high-precision probing of atomic or molecular resonance spectral lines and elegant fundamental physics experiments [5-8]. Due to its relative simplicity and reliability, this technique is known to be of relevant interest and widely used for laser frequency stabilization. Fractional frequency stabilities in the 10^{-13}–10^{-11} range at 1 s integration time have been demonstrated with lasers stabilized to cm-scale glass-blown atomic vapor cells [9-11]. Lasers frequency-stabilized onto molecular lines have also known a great success [12-14], including their recent deployment in space missions [15].

In usual saturated-absorption spectroscopy, the light-field configuration is based on two counter-propagating waves of same optical frequency ω, traveling in a vapor cell filled with atoms or molecules. The natural-linewidth sub-Doppler resonance can be detected using a photodiode at the output of the cell as a transparency peak in the bottom of a Doppler-broadened absorption profile when ω is scanned around the atom optical transition frequency ω_0 or around a middle point $(\omega_{01}+\omega_{02})/2$ between two transition frequencies (so-called crossover resonances).

In a recent study [16], the detection of sign-reversed enhanced-absorption sub-Doppler resonances has been demonstrated using dual-frequency sub-Doppler spectroscopy (DFSDS). This approach has allowed to improve the frequency stability of a diode laser [16] and contributed to improve the performance of Cs cell atomic clocks [17,18]. Moreover, since it is based on the use of a single-modulated laser, the compactness of a DFSDS-based laser system could remain comparable to the usual single-frequency saturated-absorption laser setup.

A theoretical analysis of the DFSDS technique has been reported in [19]. This study has demonstrated that the detection of the high-contrast sign-reversed sub-Doppler resonances results from several complex physical phenomena, including coherent population trapping states (CPT, [20-22]) of Zeeman sub-levels inside a single hyperfine (hf) state and between two hf-states, and velocity-selective optical pumping effects. However, this analysis was based on a simplified Λ-scheme, only considering independently a few nonlinear optical effects and then restricting to a limited qualitative understanding of the phenomenon.

In the present paper, an extended theoretical model of DFSDS is reported. We consider the real energy structure of the atom with manifold Zeeman sub-levels, the simultaneous contribution of various nonlinear effects and main relaxation processes. At the opposite of the simplified model proposed in [19], the extended model allows to predict quantitatively the properties (lineshape, height and linewidth) of sub-Doppler resonances. Evidence of spatial oscillations of the sub-Doppler resonance height with proper position of the retro-reflection mirror and the use of short-length cells is an important result of presented calculations. Experimental tests were performed using a Cs vapor micro-fabricated cell in order to evaluate the validity of the model. The experimental results are found to be well-explained by the theory.

In a last section, frequency stabilization of a diode laser using DFSDS onto a Cs microcell is reported, yielding an Allan deviation lower than 2 10^{-12} $\tau^{-1/2}$ until 10 s. These encouraging stability results are at 1 s averaging time 10 times better than laboratory-prototype microwave CPT-based chip-scale microwave atomic clocks (CSACs) [23-25], 100 times better than commercial CSACs [26] and are competitive with those of recently-reported microcell-based optical frequency references [27-29]. These encouraging results demonstrate that the DFSDS approach could be of interest for the development of a highly-integrated and high-stability microcell-based optical frequency reference.

II. THEORY

A. Problem statement

We consider a buffer-gas-free vapor cell placed in the field of two laser beams propagating in opposite directions along the quantization axis z (see Fig. 1). Each of the beams consists of two monochromatic plane waves:

$$\mathbf{E}(z,t)=\left[E_1\boldsymbol{\xi}_1 e^{ik_1 z}+E_3\boldsymbol{\xi}_3 e^{-i(k_1 z+\phi_1)}\right]e^{-i\omega_1 t}$$
$$+\left[E_2\boldsymbol{\xi}_2 e^{ik_2 z}+E_4\boldsymbol{\xi}_4 e^{-i(k_2 z+\phi_2)}\right]e^{-i\omega_2 t}+\text{c.c.} \quad (1)$$

with E_i the real amplitudes of the waves, ϕ_1 and ϕ_2 the phases of two backward waves, $\boldsymbol{\xi}_i$ the unit complex vectors of the wave polarizations, $k_{1,2}=\omega_{1,2}/c$ the wave numbers for the light waves with angular optical frequencies $\omega_{1,2}$, and "c.c." denotes the complex conjugate terms. In experiments, two resonant frequencies ω_1 and ω_2 can be obtained by modulating the light of a laser with an intensity Mach-Zehnder electro-optic modulator (EOM).

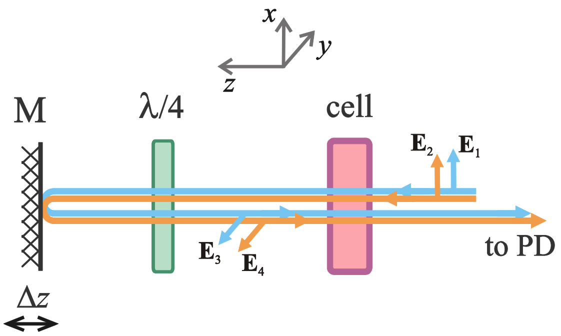

FIG. 1. Sketch of the proposed optical configuration: M: movable mirror, λ/4: quarter-wave plate, PD: photodiode.

Light waves have linear polarizations so that the components $\mathbf{E}_1$ and $\mathbf{E}_2$ are polarized along the x axis, while polarizations of the other two waves, $\mathbf{E}_3$ and $\mathbf{E}_4$, are oriented at an angle α with respect to the x axis. In spherical basis, we can write [30]:

$$\boldsymbol{\xi}_{1,2}=\left(\mathbf{e}_{-1}-\mathbf{e}_{+1}\right)/\sqrt{2}\,, \quad (2)$$

$$\boldsymbol{\xi}_{3,4}=\left(e^{i\alpha}\mathbf{e}_{-1}-e^{-i\alpha}\mathbf{e}_{+1}\right)/\sqrt{2}\,, \quad (3)$$

where complex vectors $\mathbf{e}_{\pm1}$ are spherical basis vectors responsible for σ_+ and σ_- optical dipole transitions in the atom.

Polarized light waves induce electric dipole transitions in alkali atoms, as shown in Fig. 2. For

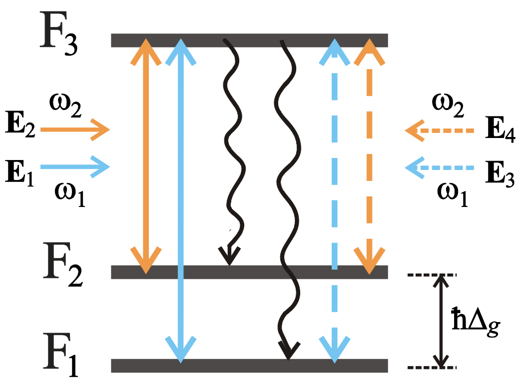

FIG. 2. Relevant energy levels of the D_1 line of an alkali atom. Solid arrows denote optical transitions induced by the waves propagating along the z-axis, while dashed arrows stand for backward waves. Wavy arrows are for spontaneous relaxation. $\hbar\Delta_g$ is the energy hyperfine splitting of the atom ground state. The case depicted here corresponds to the atoms at rest under the null Raman detuning (δ_R) and the null one-photon optical frequency detuning (δ). For Cs, we have F_1=3, F_2=F_3=4.

simplicity, the figure does not reflect the degeneracy of hyperfine levels over magnetic Zeeman sub-levels with quantum numbers $m_a = -F_a, -F_a+1, \dots, F_a$ with F_a being the total angular momentum of "a" hyperfine level (a = 1, 2, 3). This atom-light interaction leads to various nonlinear optical effects, such as optical pumping, optical transition saturation, coherences between magnetic sub-levels, and spontaneous anisotropy transfer from the excited state to the ground state. In the configuration considered here, a moving atom experiences a four-frequency light field due to the linear Doppler effect. This field induces multiple spatial harmonics of the atom's polarization. The finite size of the light beams leads also to time-of-flight relaxation. Our model includes all these effects in order to adequately reproduce the experimental observations.

The theoretical analysis is based on the standard density matrix formalism for a single atom, moving in gas. Interactions between atoms at low pressure gas can be omitted. The kinetic equation for the atom's density matrix $\hat{\rho}$ has the Lindblad form (for instance, see [1,3]):

$$\left(\frac{\partial}{\partial t}+\upsilon\frac{\partial}{\partial z}\right)\hat{\rho}=-\frac{i}{\hbar}\left[\left(\hat{V}+\hat{H}_0\right),\hat{\rho}\right]+\hat{\mathfrak{R}}\left[\hat{\rho}\right]. \quad (4)$$

Here, υ is the projection of the atom's velocity on the z axis. The operator $\hat{V}=\hat{V}_E+\hat{V}_B$ describes the interaction between the atoms and the light (E) and the static magnetic (B) fields in the electric-dipole approximation. $\hat{H}_0$ is the part of the total Hamiltonian for a free atom. The linear functional $\hat{\mathfrak{R}}$ in (4) is responsible for various relaxation processes in the atom, including the spontaneous relaxation described by the rate γ and the transit-time relaxation taken into account by the rate $\Gamma\approx\tau^{-1}$ with τbeing the mean time of the atom's passage through the light field. By introducing the latter constant, we omitted derivatives over the transverse coordinates $\partial/\partial x$ and $\partial/\partial y$ in (4). Strictly speaking, this approach corresponds to light beams with step-like intensity cross sections. This approach remainsreasonable and is widely used in theory with Gaussian-like profiles. All explicit expressions of the operators included in (4) are reported in the Appendix.

The density matrix can be expanded into series of nine matrix blocks:

$$\hat{\rho}=\sum_F \hat{\rho}_{ab}(z,t)\left|F_a\right\rangle\left\langle F_b\right| \quad (a,b=1,2,3), \quad (5)$$

where angular brackets stand for the Dirac bra- and ket-vectors. The diagonal blocks $\hat{\rho}_{aa}$ in (5) stand for magnetic sub-level populations of a single $|a\rangle$ level and coherent superpositions of these sub-levels (Zeeman coherences). $\hat{\rho}_{13}$, $\hat{\rho}_{23}$ and conjugate matrices $\hat{\rho}_{31}=\hat{\rho}_{13}^{\dagger}$, $\hat{\rho}_{32}=\hat{\rho}_{23}^{\dagger}$ are known as optical coherences since they oscillate in time at optical frequencies ω_1 and ω_2. Finally, $\hat{\rho}_{12}$ and $\hat{\rho}_{21}=\hat{\rho}_{12}^{\dagger}$ are hyperfine (hf) coherences, oscillating in time at frequencies close to Δ_g with $\hbar\Delta_g$ the ground-state hyperfine energy splitting (see Fig. 2).

The proposed light-field configuration leads to a complex dependence of the atom's polarization on the z coordinate. In this case, the matrix blocks $\hat{\rho}_{ab}(z,t)$ can be expanded into series of various spatial harmonics. Following the work presented in [19], we only consider the lowest spatial harmonics:

$$\hat{\rho}_{aa}(z)\approx\hat{\rho}_{aa}^{(0)}+\hat{\rho}_{aa}^{(+)}\,e^{2ik_{12}z}+\hat{\rho}_{aa}^{(-)}\,e^{-2ik_{12}z}\quad, \quad (6)$$

$$\hat{\rho}_{12}(z,t)\approx e^{i\delta_{12}t}\left(\hat{\rho}_{12}^{(+)}\,e^{ik_{12}z}+\hat{\rho}_{12}^{(-)}\,e^{-ik_{12}z}\right), \quad (7)$$

$$\hat{\rho}_{21}(z,t)\approx e^{-i\delta_{12}t}\left(\hat{\rho}_{21}^{(+)}\,e^{ik_{12}z}+\hat{\rho}_{21}^{(-)}\,e^{-ik_{12}z}\right), \quad (8)$$

wherek_{12}=k_1–k_2 and δ_{12}=ω_1–ω_2. Taking into account that (7) and (8) must be Hermitian conjugate to each other, we have $\hat{\rho}_{21}^{(+)\dagger}=\hat{\rho}_{12}^{(-)}$ and $\hat{\rho}_{21}^{(-)\dagger}=\hat{\rho}_{12}^{(+)}$.

Series expansions for the optical coherences are reported into the Appendix.

Many of fast spatial oscillations induced by simultaneous action of counter-propagating waves as, for instance, $e^{\pm i\,(k_1+k_2)z}, e^{\pm 2i\,k_1 z}, e^{\pm 2i\,k_2 z}$ and others, studied for various intensity ranges in [3,31,32], are dropped from our consideration for two main reasons. The first reason is that their consideration would dramatically complicate our analysis. The second reason is that experimental intensities of both counter-propagating light beams cannot be equal to each other due to losses of optical elements of the setup and light-field absorption in the cell. The latter reason is more especially confirmed in the DF regime where absorption is enhanced. Thus, the influence of higher-order spatial harmonics is significantly suppressed in the DF regime.

In (6), we show that the temporal evolution of sub-level populations is not considered since all the transient processes are assumed to be completed. The light-field interaction with the second excited-state hyperfine level F_4 (not shown in Fig. 2) of the D_1 line is neglected. This simplification can be validated since the hyperfine energy splitting in the excited state for Cs atom is large enough (1.17 GHz), compared to the Doppler profile line-width (≈370 MHz in our case).

The light-field intensity change due to absorption in the cell can be written formally as the Beer-Lambert law:

$$I_t(z_c) = I_{0t} e^{-\mathrm{OD}} \tag{9}$$

where I_{0t} is the total intensity before the cell and OD is the optical density of the medium such that:

$$\mathrm{OD} = -\int_{z_c}^{z_c+L} \chi(z)\,dz \ , \tag{10}$$

where χ is the absorption coefficient for the total light-field in the cell and z_c is the position of the cell face window along the z-axis.

The absorption coefficient depends on many parameters such as the optical frequency detuning δ, the two-photon (Raman) detuning δ_R, the polarization angle α, the relative phase $\phi_{12} = \phi_1 - \phi_2$, the coordinate z within the cell, the cell position z_c and intensities of all light waves $I_{1,2,3,4}(z)$, being also functions of the z coordinate. Instead of considering the real dependence $\chi = f(z)$ and solving the complicated Maxwell-Bloch system of equations, a proper approximate expression is used instead of (10), explained by the following assumptions. First, the alkali vapor is considered to be optically thin, i.e. OD<<1. Secondly, the coefficient χ is determined by the total population of the atom's excited state $\mathrm{Tr}\left[\hat{\rho}_{33}(z)\right]$ averaged over the Maxwellian velocity distribution. From (6), the population undergoes spatial variations due to nonlinear interference effects. Thus, χ should show the same oscillations. However, the cell length L is assumed to be much smaller than the period of these oscillations, i.e.

$$T_z = \pi/k_{12} = \pi c/\Delta_g \approx 16.3\,\mathrm{mm} >> L \approx 1.4\,\mathrm{mm} \tag{11}$$

Consequently, assuming a small optical density, the light intensity recorded by the photodetector can be written as:

$$I_t(z_c) \approx \eta I_{0t} e^{-\chi(z_c)L} \approx \eta I_{0t}\left(1-\chi(z_c)L\right), \tag{12}$$

where η stands to consider possible intensity losses on optical elements of the setup. The absorption coefficient can be expanded into two parts:

$$\chi \propto W_e = \frac{1}{\sqrt{\pi}\,\upsilon_0}\int_{-\infty}^{\infty} \mathrm{Tr}[\hat{\rho}_{33}(z_c,\upsilon)]\, e^{-\upsilon^2/\upsilon_0^2}\, d\upsilon$$

$$= W_0\left(\delta,\alpha,I_{1-4}\right) + W_z\left(\delta,\alpha,\phi_{12},I_{1-4},z_c\right) \ , \tag{13}$$

with

$$W_0 = \left\langle \mathrm{Tr}\left[\hat{\rho}_{33}^{(0)}\right]\right\rangle_\upsilon , \tag{14}$$

and

$$W_z(z) = 2\,\mathrm{sinc}\left(Lk_{12}\right)$$

$$\times\left\langle \mathrm{Re}\left\{\mathrm{Tr}\left[\hat{\rho}_{33}^{(+)}\right] e^{ik_{12}(2z_c+L)}\right\}\right\rangle_\upsilon \ , \tag{15}$$

where "sinc" is the un-normalized sinc function. The velocity $\upsilon_0 = \sqrt{2k_B T/m_a}$ in (13) is the most probable atom thermal velocity with $k_B = 1.38\times10^{-23}$ J/K the Boltzmann constant and m_a the atom's mass. Brackets $\langle\ldots\rangle_\upsilon$ stand for averaging over the Maxwellian velocity distribution.

In SDS, the light field transmitted through the vapor cell is monitored as a function of the optical frequency. In our case, this is equivalent to scanning I_t over $\delta = \omega_0 - (\omega_{31}+\omega_{32})/2$, corresponding to the optical frequency detuning of the laser carrier $\omega_0 = (\omega_1+\omega_2)/2$ from the middle frequency of both optical transitions $F_1 \rightarrow F_3$ and $F_2 \rightarrow F_3$ (see Fig. 2). As long as W_e determines all the nonlinear optical effects observed in I_t, we will analyze for different physical conditions both contributions W_0 and W_z.

Dividing the expression (13) into two parts has a real physical meaning. The term W_z is only responsible for the effects caused by hf coherences, including coherent population trapping, embracing magnetic sub-levels of different hyperfine levels F_1 and F_2. This effect is called here "hf-CPT". The term W_0 reflects all the other optical effects including optical pumping, optical transition saturation and CPT within a single level F_2. This CPT effect is called "Zeeman-CPT" since it embraces Zeeman sub-levels of a single hyperfine F_2 level. Note that as long as we consider the transition $F_1 \rightarrow F_3 = F_1 + 1$ which is not a transition of the "dark" type [33], the Zeeman-CPT does not occur within the F_1 level.

In previous studies [16,19], we have demonstrated that both Zeeman-CPT and hf-CPT effects can lead to the observation of the sub-Doppler resonance with enhanced absorption. An obvious prospect is then to predict how to make these two nonlinear effects work and add together. The simple Λ-scheme considered in [16,19] does not allow to solve this problem. Thus, the rigorous approach to discriminate the contribution of these two effects is to consider the real structureof atomic energy levels. Subsequent results are presented in the next subsections.

B. Analysis of the high-contrast effect

Let us analyze contributions W_0 and W_z in (13)in order to reveal their physical meaning and their influence on the total light field absorption in the cell under different physical conditions. In following calculations, typical parameters values of sub-Doppler spectroscopy experiments [16,19] are used, with the specificity that a miniaturized cell is considered. We consider the real structure of the Cs D_1 line with λ=894.6 nm, $\gamma = 2\pi \times 4.56$ MHz, F_1=3, F_2=4 and F_3=4 (see Fig.2). All the levels are degenerate over magnetic (Zeeman) sublevels $m = -F, -F+1, \ldots, F$. We take the time-of-flight relaxation rate $\Gamma = 0.02\gamma$, corresponding to a laser beam diameter of about 0.5 mm. The Doppler half-width is $k v_0 = 50\gamma$. For figures 3 to 6, the magnetic field is null. The Raman frequency detuning under the DF regime is assumed to be zero (δ_R=0). The optical frequency detuning δ is scanned in order to obtain the resonance curves. The absorption coefficient χ is proportional to the total excited-state population (see eq. (13)). Therefore, we focus on analyzing the population W_e as a function of the detuning δ.

Figure 3 shows numerically calculated resonances in both SF and DF regimes. When a single optical transition is excited (either $F_1 \rightarrow F_3$ or $F_2 \rightarrow F_3$, solid and dashed black curves), the regular saturated-absorption absorption dip is observed. The sign of the sub-Doppler resonance changes when the regime of excitation is switchedto the DF regime, with F_3=4 being the common excited level. In addition to the change of the resonance sign, the resonance in the DF regime is narrower and with a much higher contrast.

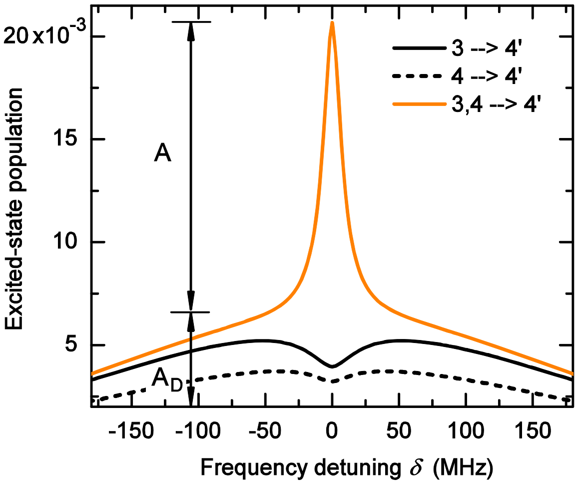

FIG. 3. Sub-Doppler resonances calculated for the single (solid and dashed curves at the bottom) and dual-frequency (solid red spike) regimes of light-field excitation. Here, A is the height of the sub-Doppler resonance under DF regime, while A_D is the height of the broad Doppler background. The total laser beam power at entrance of the cell is 50 µW. The magnetic field is switched off. Other parameters are written in the text.

1. Influence of the light wave polarizations and phases

Figure 4a shows the influence of the polarization configuration on W_0 and W_z. Both contributions, W_0 and W_z, depend in a relevant manner on the angle α between linear polarizations of the counter-propagating laser beams. For W_0, the wide Doppler background does not depend on this angle: solid green and dash-dotted blue curves overlap at their "wings" ($\delta \gg \Delta_{res}$). The sign of the resonance is not changed but its height is attenuated.

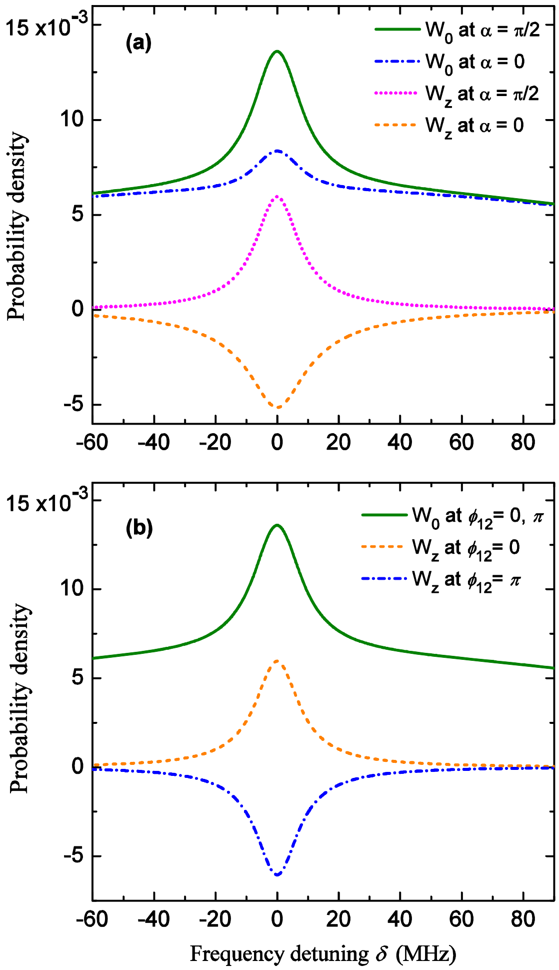

FIG. 4.Analysis of different contributions to the excited-state population. (a) Influence of linear polarizations orientation at mutual backward waves phase ϕ_{12}=0. (b) Influence of the mutual phase ϕ_{12} for orthogonal linear polarizations of the counter-propagating waves ($\alpha=\pi/2$). The total laser beam power is 50 µW, the static magnetic field B is switched off.

At the opposite, the sign of W_z strongly depends on the angle α. The absorption is enhanced for α=π/2 (orthogonal linear polarizations) whereas the transmission is increased for α=0 (parallel polarizations).When the optical detuning is large ($\delta >> \Delta_{res}$), both counter-propagating dual-frequency laser beams interact with different velocity groups of atoms and do not “feel” each other. Atoms in both groups are pumped into "non-coupled" (NC) dark states. Since these groups have different velocities, there is no “competition” between the states $|NC_1\rangle$ and $|NC_2\rangle$ and both states survive. The dark states lead to a low level of light absorption at the Doppler “wings” of the absorption profile (see solid green and dash-dotted blue curves in Fig. 4a).

At resonance ($\delta \leq \Delta_{res}$), both laser beams interact with the same atoms. The result of this interaction depends strongly on the polarization configuration since the quantum state of the atom depends on the angle α. With orthogonal polarizations ($\alpha=\pi/2$), a significant increase of W_0 and W_z is obtained (Fig. 4a, solid green and dotted pink curves, respectively). The increase of W_0 is due to the destruction of the Zeeman-CPT states. Dark states created within the F_2 level are orthogonal, i.e. $\langle NC_1|NC_2\rangle = 0$, and cancel each other. The vapor becomes less transparent for the light. The increase of W_z is caused by the destruction of the hf-CPT states.

With parallel linear polarizations, hyperfine dark states can exist but do not compete with each other. At resonance ($\delta \leq \Delta_{res}$), atoms are pumped faster into hf-CPT states due to the simultaneous action of both beams. This process causes the creation of an absorption dip in W_z (see Fig. 4a, dashed orange line). The same dip-like structure in the center of $W_0(\delta)$ picture might be expected. Indeed, if light beam polarizations are parallel (α=0), both dark states $|NC_1\rangle$ and $|NC_2\rangle$, which could be created at $\delta >> \Delta_{res}$ within the F_2 level by independent light beams, should also survive at $\delta \approx \Delta_{res}$ since these states are parallel, i.e. $\langle NC_1|NC_2\rangle = 1$. However, only a reduction of the central resonance height is observed, while its sign remains positive (see a blue dash-dotted line in Fig. 4a). The fact is that W_0 term, in contrast to W_z, includes other nonlinear effects besides creation of the CPT states. In particular, optical pumping effect also contributes to W_0. This effect can lead to increased light field absorption at $\delta \leq \Delta_{res}$ even under the parallel linear polarizations (α=0). This issue will be discussed further in the text.

Fig. 4b shows the behavior of W_0 and W_z for different values of the mutual phase ϕ_{12}. It is seen that W_0 is immune to the change of ϕ_{12} since the latter only influences hf coherences and subsequent nonlinear effects. The phase ϕ_{12} is not relevant for other effects such as optical pumping or Zeeman-CPT effects. In contrast, the sign of W_z strongly depends on ϕ_{12}. For ϕ_{12} = π/2, hyperfine dark states cancel each other and increased absorption is observed. The opposite case is observed for W_z with ϕ_{12} = 0, when dark states are parallel to each other. Note that the dependence of W_e on the polarization angle α and the relative phase ϕ_{12} could be also treated using the general theory of closed contours

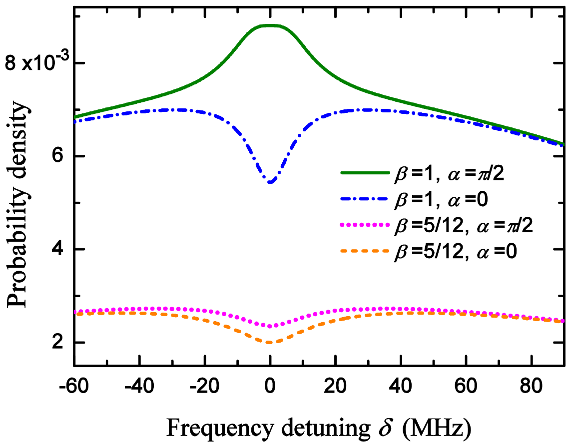

FIG. 5. Calculated contribution W_0 in the single-frequency regime, when only the transition $F_2 \rightarrow F_3$ is excited. β is the branching ratio for the transition. The total laser beam power is 50 µW. The static magnetic field is null.

described in [34]. Common points have also been treated for the study of sub-natural electromagnetically induced transparency and absorption resonances in [35,36] for the hf-CPT states and in [37,38] for the Zeeman-CPT states.

2. Influence of the transition openness

Let's consider first the case where the SF regime is used. Fig. 5 reports the evolution of W_0 when only the $F_2 \rightarrow F_3$ transition is excited. The coefficient β $(0 \leq \beta \leq 1)$ noted in Fig. 5 is the branching ratio and characterizes the openness of the transition. In particular, β=1 corresponds to a closed transition without any spontaneous decay to other non-resonant hyperfine levels (as F_1). Fig. 5 shows that the sign-reversal effect (increased absorption) should be observed for a closed transition (β=1), with α=π/2. Indeed, with β=1, the Zeeman-CPT effect occurs and can lead to the observation of an absorption peak-like resonance. At the opposite, if the transition is noticeably open (this is the case for F_2=4→F_3=4 in Cs with β=5/12), the Zeeman-CPT effect is significantly suppressed. In this case, no sign-reversal of the traditional sub-Doppler resonance structure is observed, whatever the polarization configuration ($\alpha=\pi/2$ or 0).

At the opposite, as shown in Fig. 4a (solid green and dash-dotted blue curves), the Zeeman-CPT effect contributes to the absorption peak observation in the DF regime, when both optical transitions are excited. In other words, the Zeeman-CPT effect does not work in the SF regime (Fig. 5) while it is again in action in the DF regime. This phenomenon is explained by the presence of the second field, resonant with the $F_1 \rightarrow F_3$ transition, able to optically-pump atoms back into the F_2 level. The second field plays here the role of an optical repumper and increases the effective branching ratio for the $F_2 \rightarrow F_3$ transition..

At α=0 the Zeeman CPT states contribute to reduction of light absorption in W_0 in Fig. 4a (compare solid green and dash-dotted blue curves). However, these states do not lead to observation of any absorption dip at the resonance center in W_0 as it can be intuitively expected. The reason is that a regular optical pumping effect prevents the change of the resonance sign. When both counter-propagating beams interact with the same atoms ($\delta \leq \Delta_{res}$), more atoms are pumped to the F_2=4 level from the F_1=3 level and the absorption increases, in spite of many (not all) of the atoms are accumulated in the dark state within the F_2=4 level.

3. Influence of the imbalance between counter-propagating light wave intensities

Figure 6 depicts the influence on W_0 and W_z of the light wave intensities imbalance. The contribution of both hyperfine-CPT and Zeeman-CPT effects to the absorption peak observation is optimized in the case where both counter-propagating beams have the same intensity. This condition is the best one to destroy the CPT states of the atom at the resonance center ($\delta \leq \Delta_{res}$) and then to increase the light field absorption. It is well shown in Fig. 6 that the intensity imbalance affects the strength of the central absorption peak.

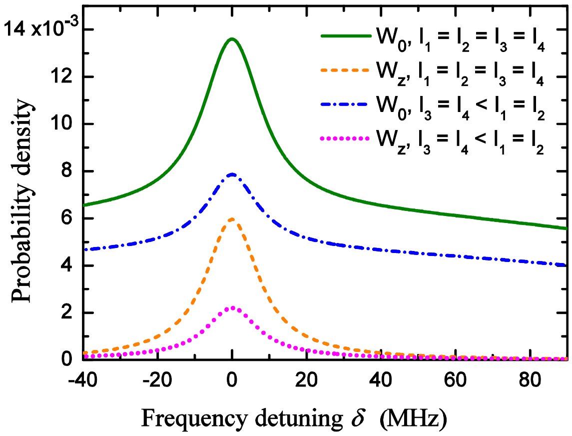

FIG. 6. Influence of a difference in light wave intensities on W_0 and W_z. Parameters: ϕ_{12}=0, $\alpha=\pi/2$. The total laser beam power is 50 µW, B=0. Intensities I_3 and I_4 are assumed to be smaller than I_1 and I_2 by 30%.

4. Influence of an ambient static magnetic field

Figure 7 analyses the influence of a static magnetic field applied along the wave vectors (**B**||*z*). We consider here the associated Larmor frequency $\Omega\equiv\Omega_2=g_2\mu_B B/\hbar$ with g_2 the Landé *g*-factor of the F_2 level and μ_B=927.4×10^{-26} J/T the Bohr magneton. This Larmor frequency is different for different energy levels and is responsible for linear shifts of magnetic sub-levels *m* under the external magnetic field. For an alkali atom, we note $\Omega_1= -\Omega_2$ and $\Omega_3= (g_3/g_2)\Omega_2$.

As already discussed, the strong light absorption is observed under two mutually orthogonally polarized counter-propagating beams due to presence of the Zeeman CPT states in the atoms within the F_2 level at $\delta>>\Delta_{\text{res}}$ and destruction of the states at $\delta\leq\Delta_{\text{res}}$. When a static magnetic field is applied, Zeeman sublevels of the F_2 are frequency shifted and the dark states are not created, whatever the value of the detuning δ and polarization configuration (see blue dash-dotted curves in Fig. 7a,b). The magnetic field leads to the creation of an absorption dip in the center of the W_0 profile due to the regular saturated absorption effect.

Concerning W_z (see orange dashed and pink dotted curves in Fig. 7b), the application of the magnetic field does not lead to the total destruction of the absorption-peak effect. The peak in W_z is still possible due to the fact that some Λ-schemes, embracing magnetic sub-levels of different hyperfine states (F_1 and F_2), are insensitive to weak magnetic fields. It means that the hf-CPT effect partly survives, which can be a reason for the absorption peak observation (also, see [19]).

5. Interest of short-length cells

In the end of this section, we emphasize that the contribution W_z to the absorption coefficient falls off with the cell length as sinc($k_{12}L$) (see eq. (15)). It means that the impact of W_z contribution can be increased by using short-length vapor cells instead of extended-length cells which usually preferable for regular saturated-absorption technique.

The contribution W_z also depends on the cell position with respect to the retro-reflection mirror (see Fig. 1). This position should be optimized to guarantee observation of the highest sub-Doppler resonance. This interesting feature is demonstrated experimentally in the next section.

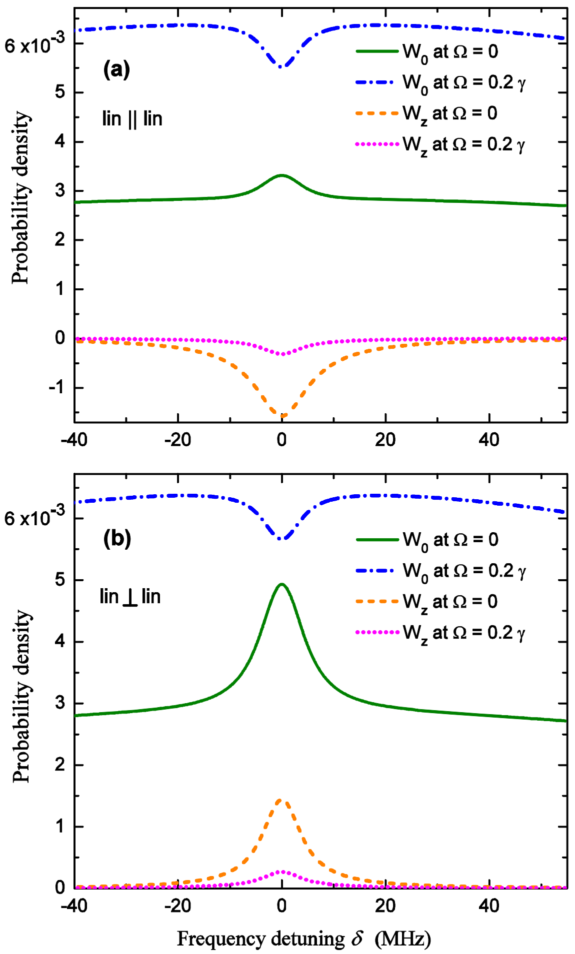

FIG. 7. Influence of the static magnetic field on W_0 and W_z. The field is applied along the light wave vectors (*z* axis) at (a) parallel and (b) orthogonal linear polarizations of counter-propagating laser beams. Parameters are: P = 10 μW and ϕ_{12}=0. Ω is the Larmor frequency.

III. SPECTROSCOPY EXPERIMENTS

A. Setup

The heart of the experiment, shown on Fig. 8a, is a Cs vapor micro-fabricated cell analog to the one described in [39,40,24]. The sub-Doppler spectroscopy takes place in a 2-mm diameter and 1.4-mm long cylindrical cavity. The cell does not contain any buffer gas. The cell is temperature-stabilized and is placed inside a cylindrical μ-metal magnetic shield. The optical setup is shown in Fig. 8b. The light source is a narrow-linewidth external cavity diode laser (ECDL) tuned to the Cs D_1 line. The laser output beam is connected to a fibered Mach-Zehnder EOM. For DFSDS tests, the EOM is modulated using a commercial microwave frequency synthesizer by a 4.596 GHz signal in order to produce two optical sidebands frequency-split by 9.192 GHz. The laser carrier is then

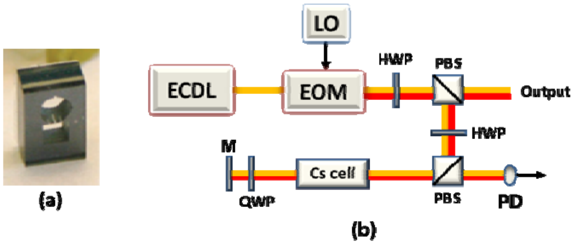

FIG. 8. (a): Photograph of a Cs micro-fabricated vapor cell. (b) Experimental setup for DFSDS measurements in the Cs microcell. ECDL: external-cavity diode laser, EOM: electro-optic modulator, LO: 4.596 GHz microwave synthesizer, HWP: half-wave plate, PBS: polarizing beam splitter, QWP: quarter-wave plate, M: mirror, PD: photodiode. The 4.596 GHz signal is applied to the EOM for the dual-frequency measurements.

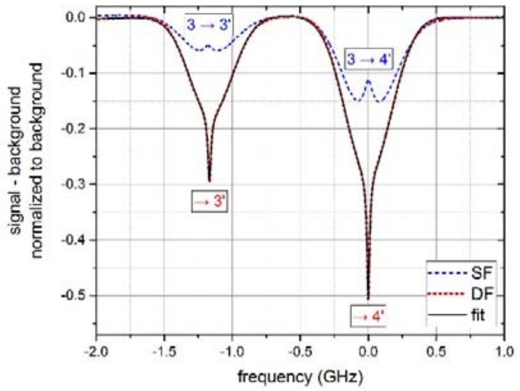

FIG. 9. Measurements of single-frequency (SF) and dual-frequency (DF) sub-Doppler spectra through the microcell at 60°C. The laser power is about 200 μW after a single pass. The SF spectrum obtained from the F_1=3 state. The spectra are fitted by 2-Doppler plus 2-Lorentzian functions with a quadratic background. Fit parameters for similar scans were used to deduce the height and width of the Doppler-broadened and sub-Doppler profiles.

actively suppressed using the method described in [36]. For standard SFSDS tests, the EOM is not modulated. Before entering the cell, the light beam passes two half-wave plates and two polarizing beam splitters ensuring power control and linear polarization in the cell. The beam is sent into the cell, retro-reflected using a mirror through the cell and detected at the output by a photodiode for the detection of the sub-Doppler resonance. The mirror is placed onto a translation stage. A quarter-wave plate between the cell and the reflection mirror ensures that both counter-propagating beams are mutually orthogonally polarized. The width of the light beam is about 0.45 mm.

Figure 9 shows typical sub-Doppler spectra detected in the micro-fabricated cell at 60°C. In the single-frequency (SF) regime, we observe the standard saturated-absorption resonances with increased transmission of the light through the vapor when the laser frequency is resonant with the atomic optical transitions. In the dual-frequency (DF) regime, as reported in [16,19] with cm-scale cells, a significant sign-reversal effect of the sub-Doppler resonance is observed and a narrow and high-contrast absorption spike is obtained.

B. Measurements

Fig.10 shows the oscillations of the sub-Doppler resonance height in the DF regime versus the reflection mirror position. This effect, predicted in our previous study [19] and here by eq. (15), is explained by the dependence of the excited-state population on the *z*-coordinate of the cell. This dependency results from slow spatial oscillations of the hyperfine coherences, explaining that the position of the cell can be optimized to maximize the W_z contribution to the absorption peak creation. On Fig. 10, experimental data points are compared to numerical calculations based on the density matrix formalism.

We analyze on Fig. 10 the resonance height A normalized to the Doppler background height A_D (see Fig. 3). It is seen that the resonance height can be even larger than the height of the broad Doppler resonance. Such a high relative contrast of the sub-Doppler resonance (>100%) is not possible in standard SF spectroscopy setups in which relative contrast usually does not exceed 20–30%.

The discrepancy between the experimental data and theory in Fig. 10 can be explained by several reasons. A first reason is the non-negligible optical thickness of the medium, neglected in our theory. A second reason is that the reflected beam undergoes intensity oscillations together with the oscillations of the light absorption in the cell. This means that different positions of the mirror provide different combinations of forward and backward light beam intensities. In order to consider this effect correctly, a solution of the full system of Maxwell-Bloch equations would be needed. Another reason is linked with the influence of the high-order spatial harmonics of atom's polarization at $I \geq I_{sat}$ with I_{sat} being the saturation intensity (~mW/cm^2). In the theory, we consider only the lower harmonics as it is seen from eqs. (6)–(8) and (A13)–(A14).We note again that such spatial oscillations of the sub-

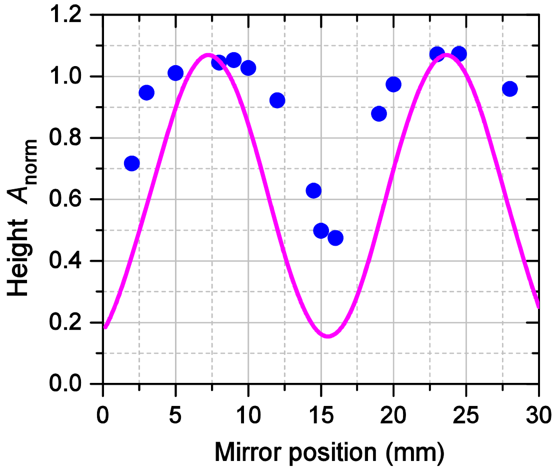

FIG. 10. Height of the sub-Doppler absorption spike normalized to the Doppler background height versus the distance between the retro-reflection mirror and the microcell (Fig. 8). The solid line is the result of numerical calculations. The cell temperature is 42°C. The laser is connected to the F_3=4 excited state and the laser power is 45 μW.

Doppler resonance height cannot be easily revealed in cm-scale cells, as explained in Section II-A and mentioned in [19]. This observation is notably highlighted in short-length vapor cells.

Figure 11 shows experimental results and calculations of the resonance line-width and normalized height in both SF and DF regimes versus the total laser power. In the DF regime, experimental results are reported for two different temperatures (42°C and 60°C). Note that in experiments, intensities of the backward waves $\mathbf{E}_{3,4}$ are not equal to those of incident waves $\mathbf{E}_{1,2}$ (see sketch in Fig. 1) due to absorption of light in the cell and different losses on the beam path. To take this into account into the model, we consider the following relations in our calculations: I_1=I_2, I_3=I_4=$0.5I_1$.

In experiments, the measured line-width of the resonance (see Fig. 11a) in the DF case is several times smaller than in the SF case and found to be closer to the natural line-width when extrapolated at zero intensity. For a total laser power of about 70 μW, the resonance FWHM is 59.1 MHz in the SF regime while it is 16 MHz in the DF case.

In the DF regime, experimental data are well fitted by numerical calculations. In the SF regime, the discrepancy between experience and theory can be explained by the same reasons than noted for Fig.10. In particular, the role of high-order spatial harmonics of atom's polarization can be more relevant in the SF regime rather than in the DF regime of interaction. Additionally, experimental

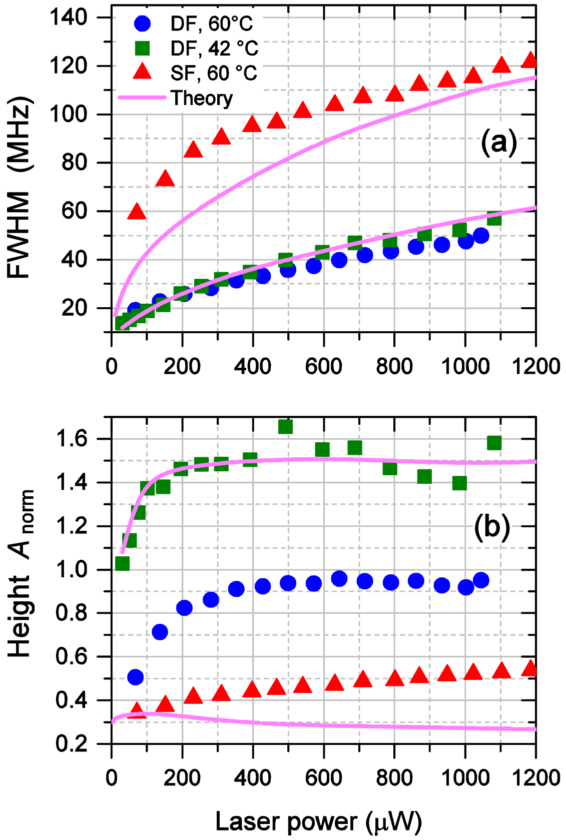

FIG. 11. (a) Linewidth and (b) normalized height of the sub-Doppler resonance as a function of the laser power under the single-frequency (SF) and dual-frequency (DF) regimes. Theory results are shown as solid curves. In SF regime, the transition F_1=3→F_3=4 is excited. Other parameters are: α=π/2, ϕ_{12}=0, B=0.

data for the resonance width might contain a residual Doppler broadening due to minor imperfections in alignment of the beams [41].

The line-width in both SF and DF regimes exhibits a well-known square-root-like behavior [3,41]: $\mathrm{FWHM} \propto \gamma\sqrt{1+G}$, with G being the effective saturation parameter. At the same time, the nonlinear resonance in the DF regime is significantly narrower. This can be explained on the basis of a simplified two-level model of the atom [42]. Broadening of the sub-Doppler resonance in the SF regime results from the transition openness. In the DF regime, at $\delta \approx \Delta_{\mathrm{res}}$ and orthogonal linear polarizations, the effective two-level scheme is closed since there are no trap states to accumulate the atoms.

Figure 11.(b) shows that the height of the sub-Doppler resonance in the DF regime is about three times larger than in the SF case for a similar cell temperature of 60°C. In the DF case, experimental data are in good agreement with the theory.

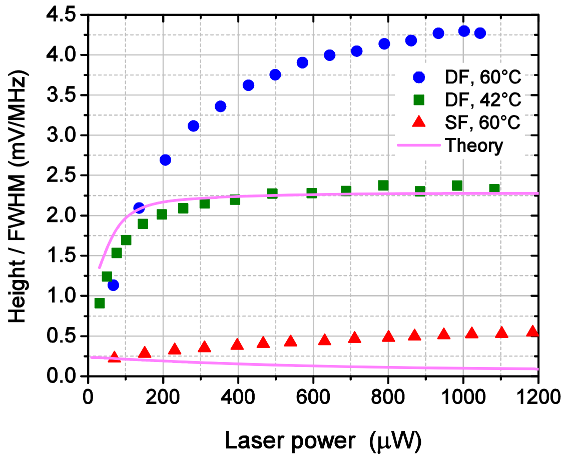

FIG. 12. Non-normalized height of the resonance divided by its linewidth versus laser power under the single-frequency (SF) and dual-frequency (DF) regimes.

The height of the resonance is maximized for a laser power of about 600 μW at 60°C and can be 1.5 times higher than the broad Doppler background. The influence of temperature on the resonance height is obvious. A higher temperature leads to increased optical thickness of the vapor and considerable light wave absorption in the cell. The latter increases the imbalance between forward and backward light beam intensities. As discussed in Section II-B, this situation does not help to observe a higher-contrast normalized resonance.

In the SF regime, the resonance height increases slightly up to 1200 μW. For power values lower than 20 μW, the experimental data agree with the theory. For higher powers, the observed discrepancy could be caused by the influence of the high-order harmonics as for Fig. 10.

Figure 12 shows the non-normalized height of the resonance divided by FWHM. This figure of merit is important for laser frequency stabilization. For a cell temperature of 60°C, the height/FWHM ratio in the DF case can be about a factor 8 higher than in the SF regime.

IV. FREQUENCY STABILIZATION

In a last step, inspired by results observed in Fig. 12, we have measured the fractional frequency stability of a laser beat-note between two laser systems. The first laser system (LS1) is the one described in Fig. 8. The second laser system (LS2), similar to that described in [16], is based on the same principle but uses a distributed feedback (DFB) diode laser (instead of an ECDL) and a cm-scale Cs cell (instead of a microcell). For all measurements, the laser LS2 is stabilized using the DFSDS technique. The laser LS1 can be stabilized using DFSDS or SFSDS regimes. In order to create a laser beat-note between both lasers, the laser beam at the EOM output of LS2 is sent into an acousto-optic modulator (AOM), shifting by 122 MHz the dual-frequency optical field. The resulting output beam is superimposed using a cube with the beam from the LS1 laser direct output (before EOM). A microwave beat-note signal at 4.596 GHz +/- 122 MHz is detected with a fast photodiode. A single beat-note component is then filtered using a 40 MHz-bandwidth microwave band-pass filter and amplified by 40 dB. This signal is then mixed with a 4.496 GHz signal delivered by a commercial microwave synthesizer driven by a reference hydrogen maser. The final 22 MHz signal at the output of the mixer is finally low-pass filtered, amplified and counted with a frequency counter.

Figure 13 reports the Allan deviation of the beat-note between both laser systems, with the microcell-stabilized laser (LS1) in different regimes. In each case (SF and DF), the laser power of LS1 is adjusted to a value where the ratio height/FWHM is optimized (400 μW in the SF case, 1 mW in the DF case).

In the DF regime, the short-term frequency stability is measured to be $2\times10^{-12}\ \tau^{-1/2}$ until about 10 s. These performances are about a factor 4 better than those obtained in the SF regime. This factor of 4 is lower than the one observed on the height/FWHM ratio (see Fig. 12). This could be explained by a more favorable detection noise level in the SF regime since the operating laser power is

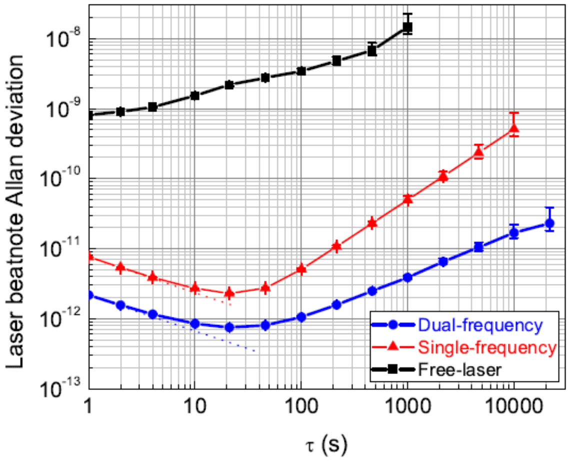

FIG. 13. Allan deviation of the laser beat-note for free-running (black squares), single-frequency (red triangles), and dual-frequency (blue circles) regimes. In the SF case, the transition $F_1=3\rightarrow F_3=4$ is excited.

lower in this case. These aspects will be studied in more detail in future investigations. For τ > 20 s, the laser stability in the DFSDS case is degraded with a $\tau^{+1/2}$ frequency random walk signature, yielding 1.5×10^{-11} at 10^4 s. Main contributions to this degradation are out of the scope of this paper and deserve a dedicated further study.

While at a preliminary stage of study and characterization, the short-term stability of the DFSDS microcell-based laser is at 1 s about 100 times better than those of commercial CPT-based chip-scale microwave atomic clocks [26] and competitive with recently-reported microcell-based optical frequency references [27-29]. These encouraging results demonstrate that the DFSDS approach could be, if combined with integrated laser, photonics and microwave technologies, an interesting alternative option for the development of a new-generation ultra-compact and high-stability microcell-based optical frequency reference.

V. CONCLUSIONS

We have developed an extended theoretical model to describe the effect of high-contrast sub-Doppler resonances observed under the dual-frequency regime in alkali vapor cells. This theory generalizes the previous qualitative simplified models proposed in [16,19]. The extended model considers the real structure of atomic energy levels and various nonlinear optical phenomena. Experimental results were performed to validate the model using a Cs vapor microcell. Oscillations of the sub-Doppler resonance height with translation of the reflection mirror position have been demonstrated. The impact of the laser intensity and cell temperature on the sub-Doppler resonance properties has been studied in both SF and DF regimes. Experimental results are well explained by the theory and rigorous explanations were suggested to explain discrepancies. The interest of the DFSDS approach for laser frequency stabilization has been pointed out. A laser beat-note between two laser systems, including one stabilized by the DFSDS technique with a Cs microcell, has demonstrated an Allan deviation of 2×10^{-12} at 1 s. These results suggest that the DFSDS approach could be of interest for the development of a highly-integrated and high-stability microcell-based optical frequency reference.

ACKNOWLEDGMENTS

This work has been supported by Région Bourgogne Franche-Comté and Labex FIRST-TF. We thank the platformOscillator-Imp for the distribution of a reference hydrogen masersignal in the laboratory.The authors thank C. Rocher and P. Abbé (FEMTO-ST) for their help with experimental work andelectronics. The work of D. Brazhnikov was supported by Russian Science Foundation (grant no. 17-72-20089).

APPENDIX

Let us provide explicit expressions for the operators from (4). The free-atom Hamiltonian is:

$$\hat{H}_0 = \sum_{F_a, m_a} \varepsilon_a \left| F_a, m_a \right\rangle \left\langle F_a, m_a \right| \,, \qquad \text{(A1)}$$

whereε_a is the energy of F_a level with a = 1,2,3.

The light-atom interaction operator $\hat{V}_E$ is

$$\hat{V}_E = -\hbar \begin{pmatrix} \hat{0} & \hat{0} & \hat{V}_{31}^{\dagger} e^{i\omega_1 t} \\ \hat{0} & \hat{0} & \hat{V}_{32}^{\dagger} e^{i\omega_2 t} \\ \hat{V}_{31} e^{-i\omega_1 t} & \hat{V}_{32} e^{-i\omega_2 t} & \hat{0} \end{pmatrix} . \qquad \text{(A2)}$$

In the rotating-wave and electric-dipole approximations, the matrix blocks in (A2) are:

$$\hat{V}_{31} = R_1 \hat{\Upsilon}_{31}^{(1)} e^{ik_1 z} + R_3 \hat{\Upsilon}_{31}^{(3)} e^{-i(k_1 z + \phi_1)} , \qquad \text{(A3)}$$

$$\hat{V}_{32} = R_2 \hat{\Upsilon}_{32}^{(2)} e^{ik_2 z} + R_4 \hat{\Upsilon}_{32}^{(4)} e^{-i(k_2 z + \phi_2)} , \qquad \text{(A4)}$$

with R_i the Rabi frequencies and $\hat{\Upsilon}_{3a}^{(j)}$ (a =1,2, j=1–4) the dimensionless interaction operators. According to the Wigner-Eckart theorem, we have:

$$\hat{\Upsilon}_{3a}^{(j)} = \boldsymbol{\xi}_j \cdot \hat{\mathbf{T}}^{3a} , \qquad \text{(A5)}$$

where$\boldsymbol{\xi}_j$ is the j-wave polarization vector from (2) and (3). The q-components of operators $\hat{\mathbf{T}}^{3a}$ are:

$$\hat{T}_q^{3a} = \sum_{m_3, m_a} (-1)^{F_3 - m_3} \begin{pmatrix} F_3 & 1 & F_a \\ -m_3 & q & m_a \end{pmatrix} \times \left| F_3, m_3 \right\rangle \left\langle F_a, m_a \right| , \qquad \text{(A6)}$$

with (…) being the $3jm$-symbols [30].

The interaction of atoms with the magnetic field is described by

$$\hat{V}_B = \hbar\Omega \begin{pmatrix} -\hat{F}_1 & \hat{0} & \hat{0} \\ \hat{0} & \hat{F}_2 & \hat{0} \\ \hat{0} & \hat{0} & (g_3/g_2)\hat{F}_3 \end{pmatrix}, \qquad \text{(A7)}$$

where Ω is the Larmor frequency of the F_2 level. Here, the dimensionless operators $\hat{F}_a$ stand for the *z*-projections of operators of total angular momentum in F_a level. In the basis of eigenstates of the free-atom Hamiltonian $\hat{H}_0$, these operators have simple diagonal form:

$$\hat{F}_a = \sum_{m_a=-F_a,..,F_a} m_a \left|F_a,m_a\right\rangle\left\langle F_a,m_a\right| , \qquad \text{(A8)}$$

The part of operator $\hat{\mathfrak{R}}$ in (4) responsible for the spontaneous relaxation is:

$$\hat{\mathfrak{R}}^{\text{spon}} = \gamma(2F_3+1) \sum_{\substack{a=1,2 \\ q=0,\pm1}} \beta_{3a}\, \hat{T}_q^{3a\dagger}\, \hat{\rho}^{aa} \hat{T}_q^{3a} , \qquad \text{(A9)}$$

where γ is the spontaneous relaxation rate and β_{3a} the branching ratios:

$$\beta_{3a} = (2J_e+1)(2F_a+1)\begin{Bmatrix} J_g & I_{\text{n}} & F_a \\ F_3 & 1 & J_e \end{Bmatrix}^2 , \qquad \text{(A10)}$$

where $J_{\text{e,g}}$ are the total angular momenta of electrons in excited (e) and ground (g) atomic states, I_{n} is the nuclear spin and {…} stands for the 6*j*-symbol [30]. Obviously, $\beta_{31}+\beta_{32}=1$. For the D_1 line of Cs atom, we have $J_{\text{g}}=J_{\text{e}}=1/2$ and $I_{\text{n}}=7/2$.

The time-of-flight relaxation term is

$$\hat{\mathfrak{R}}^{\text{flight}} = \Gamma\left[\hat{\rho}^{\text{isotr}} - \hat{\rho}\right], \qquad \text{(A11)}$$

The magnetic sub-levels of both ground-state levels F_1 and F_2 (see Fig. 2) are populated isotropically when atoms are beyond the light field. This initial state is described by the following matrix:

$$\hat{\rho}^{\text{isotr}} = (2I_{\text{n}}+1)^{-1} \sum_{a=1,2} \left|F_a,m_a\right\rangle\left\langle F_a,m_a\right| . \qquad \text{(A12)}$$

The optical coherences can be expended into the series (see also [19]):

$$\hat{\rho}_{13}(z,t) = e^{i\omega_1 t}\Big(\hat{\rho}_{13}^{(-1)}\, e^{-ik_1 z} + \hat{\rho}_{13}^{(+1)}\, e^{i(k_1 z+\phi_1)}$$
$$+\hat{\rho}_{13}^{(-21)}\, e^{-i(2k_2-k_1)z} + \hat{\rho}_{13}^{(+21)}\, e^{i(2k_2-k_1)z+i\phi_1}\Big), \qquad \text{(A13)}$$

$$\hat{\rho}_{23}(z,t) = e^{i\omega_2 t}\Big(\hat{\rho}_{23}^{(-2)}\, e^{-ik_2 z} + \hat{\rho}_{23}^{(+2)}\, e^{i(k_2 z+\phi_2)}$$
$$+\hat{\rho}_{23}^{(-12)}\, e^{-i(2k_1-k_2)z} + \hat{\rho}_{23}^{(+12)}\, e^{i(2k_1-k_2)z+i\phi_2}\Big). \qquad \text{(A14)}$$

Similar expansions can be written for Hermitian conjugate matrices $\hat{\rho}_{31} = \hat{\rho}_{13}^{\dagger}$ and $\hat{\rho}_{32} = \hat{\rho}_{23}^{\dagger}$.

The static magnetic field *B*, if present in the vapor cell, is assumed to be small enough to satisfy the condition $\Omega \ll \gamma$. This allows to take into account the magnetic field influence only on the ground-state levels. This means that the Zeeman splitting of the saturated-absorption resonance does not occur, while the influence of the *B*-field on creation of the Zeeman-CPT effect is considered.

All the listed assumptions help us exclude the optical coherences from the final system of equations. In particular, we have for the matrix harmonics of the ground state F_1:

$$\left(\Gamma + R_1^2 L_1^{(-)*}\hat{\Upsilon}_{13}^{(1)}\hat{\Upsilon}_{31}^{(1)} + R_3^2 L_1^{(+)*}\hat{\Upsilon}_{13}^{(3)}\hat{\Upsilon}_{31}^{(3)}\right)\hat{\rho}_{11}^{(0)}$$
$$+\hat{\rho}_{11}^{(0)}\left(R_1^2 L_1^{(-)}\hat{\Upsilon}_{13}^{(1)}\hat{\Upsilon}_{31}^{(1)} + R_3^2 L_1^{(+)}\hat{\Upsilon}_{13}^{(3)}\hat{\Upsilon}_{31}^{(3)}\right)$$
$$-2\gamma_{eg} S_{11}^{(-)}\hat{\Upsilon}_{13}^{(1)}\hat{\rho}_{33}^{(0)}\hat{\Upsilon}_{31}^{(1)} - 2\gamma_{eg} S_{31}^{(+)}\hat{\Upsilon}_{13}^{(3)}\hat{\rho}_{33}^{(0)}\hat{\Upsilon}_{31}^{(3)}$$
$$+R_1R_2L_1^{(-)*}\hat{\Upsilon}_{13}^{(1)}\hat{\Upsilon}_{32}^{(2)}\hat{\rho}_{21}^{(+)} + R_3R_4L_1^{(+)}\hat{\rho}_{12}^{(+)}\hat{\Upsilon}_{23}^{(4)}\hat{\Upsilon}_{31}^{(3)}e^{-i\phi_{12}}$$
$$+R_1R_2L_1^{(-)}\hat{\rho}_{12}^{(-)}\hat{\Upsilon}_{23}^{(2)}\hat{\Upsilon}_{31}^{(1)} + R_3R_4L_1^{(+)*}\hat{\Upsilon}_{13}^{(3)}\hat{\Upsilon}_{32}^{(4)}\hat{\rho}_{21}^{(-)}e^{i\phi_{12}}$$
$$-i\Omega\left[\hat{F}_1,\hat{\rho}_{11}^{(0)}\right] - \hat{\mathfrak{R}}_{11}^{\text{spon}}\left\{\hat{\rho}_{33}^{(0)}\right\} = \Gamma\,\hat{\rho}_{11}^{\text{isotr}} , \qquad \text{(A15)}$$

$$\left(\Gamma + 2ik_{12}\upsilon + R_3^2 M_1^{(+)*}\hat{\Upsilon}_{13}^{(3)}\hat{\Upsilon}_{31}^{(3)}\right)\hat{\rho}_{11}^{(+)}$$
$$+R_1^2 M_1^{(-)}\hat{\rho}_{11}^{(+)}\hat{\Upsilon}_{13}^{(1)}\hat{\Upsilon}_{31}^{(1)} - i\Omega\left[\hat{F}_1,\hat{\rho}_{11}^{(+)}\right] - \hat{\mathfrak{R}}_{11}^{\text{spon}}\left\{\hat{\rho}_{33}^{(+)}\right\}$$
$$-R_1^2 M_1^{(-)}\hat{\Upsilon}_{13}^{(1)}\hat{\rho}_{33}^{(+)}\hat{\Upsilon}_{31}^{(1)} - R_3^2 M_1^{(+)*}\hat{\Upsilon}_{13}^{(3)}\hat{\rho}_{33}^{(+)}\hat{\Upsilon}_{31}^{(3)}$$
$$+R_1R_2M_1^{(-)}\hat{\rho}_{12}^{(+)}\hat{\Upsilon}_{23}^{(2)}\hat{\Upsilon}_{31}^{(1)}$$
$$+R_3R_4M_1^{(+)*}\hat{\Upsilon}_{13}^{(3)}\hat{\Upsilon}_{32}^{(4)}\hat{\rho}_{21}^{(+)}e^{i\phi_{12}} = 0 . \qquad \text{(A16)}$$

Here and after square brackets with comma […,…] stand for the commutation operation of two matrices. Also, as long as $\hat{\rho}_{11}^{(-)} = \hat{\rho}_{11}^{(+)\dagger}$, the equation for matrix $\hat{\rho}_{11}^{(-)}$ can be easily derived from (A16). Similarly, we get for the ground state F_2:

$$\left(\Gamma + R_2^2 L_2^{(-)*}\hat{\Upsilon}_{23}^{(2)}\hat{\Upsilon}_{32}^{(2)} + R_4^2 L_2^{(+)*}\hat{\Upsilon}_{23}^{(4)}\hat{\Upsilon}_{32}^{(4)}\right)\hat{\rho}_{22}^{(0)}$$
$$+\hat{\rho}_{22}^{(0)}\left(R_2^2 L_2^{(-)}\hat{\Upsilon}_{23}^{(2)}\hat{\Upsilon}_{32}^{(2)} + R_4^2 L_2^{(+)}\hat{\Upsilon}_{23}^{(4)}\hat{\Upsilon}_{32}^{(4)}\right)$$
$$-2\gamma_{eg} S_{22}^{(-)}\hat{\Upsilon}_{23}^{(2)}\hat{\rho}_{33}^{(0)}\hat{\Upsilon}_{32}^{(2)} - 2\gamma_{eg} S_{42}^{(+)}\hat{\Upsilon}_{23}^{(4)}\hat{\rho}_{33}^{(0)}\hat{\Upsilon}_{32}^{(4)}$$
$$+R_1R_2L_2^{(-)*}\hat{\Upsilon}_{23}^{(2)}\hat{\Upsilon}_{31}^{(1)}\hat{\rho}_{12}^{(-)} + R_3R_4L_2^{(+)}\hat{\rho}_{21}^{(-)}\hat{\Upsilon}_{13}^{(3)}\hat{\Upsilon}_{32}^{(4)}e^{i\phi_{12}}$$
$$+R_1R_2L_2^{(-)}\hat{\rho}_{12}^{(+)}\hat{\Upsilon}_{13}^{(1)}\hat{\Upsilon}_{32}^{(2)} + R_3R_4L_2^{(+)*}\hat{\Upsilon}_{23}^{(4)}\hat{\Upsilon}_{31}^{(3)}\hat{\rho}_{12}^{(+)}e^{-i\phi_{12}}$$

$$+i\Omega\left[\hat{F}_2,\hat{\rho}_{22}^{(0)}\right]-\hat{\mathfrak{R}}_{22}^{\mathrm{spon}}\left\{\hat{\rho}_{33}^{(0)}\right\}=\Gamma\,\hat{\rho}_{22}^{\mathrm{isotr}}, \quad \text{(A17)}$$

$$\begin{aligned}
&\left(\Gamma+2ik_{12}\upsilon+R_2^2M_2^{(-)*}\hat{\Upsilon}_{23}^{(2)}\hat{\Upsilon}_{32}^{(2)}\right)\hat{\rho}_{22}^{(+)}\\
&+R_4^2M_2^{(+)}\hat{\rho}_{22}^{(+)}\hat{\Upsilon}_{23}^{(4)}\hat{\Upsilon}_{32}^{(4)}+i\Omega\left[\hat{F}_2,\hat{\rho}_{22}^{(+)}\right]-\hat{\mathfrak{R}}_{22}^{\mathrm{spon}}\left\{\hat{\rho}_{33}^{(+)}\right\}\\
&-R_2^2M_2^{(-)*}\hat{\Upsilon}_{23}^{(2)}\hat{\rho}_{33}^{(+)}\hat{\Upsilon}_{32}^{(2)}-R_4^2M_2^{(+)}\hat{\Upsilon}_{23}^{(4)}\hat{\rho}_{33}^{(+)}\hat{\Upsilon}_{32}^{(4)}\\
&+R_1R_2M_2^{(-)*}\hat{\Upsilon}_{23}^{(2)}\hat{\Upsilon}_{31}^{(1)}\hat{\rho}_{12}^{(+)}\\
&\qquad+R_3R_4M_2^{(+)}\hat{\rho}_{21}^{(+)}\hat{\Upsilon}_{13}^{(3)}\hat{\Upsilon}_{32}^{(4)}e^{i\phi_{12}}=0. \qquad \text{(A18)}
\end{aligned}$$

The Hermitian conjugation of (A18) leads to the equation for $\hat{\rho}_{22}^{(-)}$.

Following equations are for the upper state:

$$\begin{aligned}
&\left(\Gamma+\gamma+R_1^2L_1^{(-)}\hat{\Upsilon}_{31}^{(1)}\hat{\Upsilon}_{13}^{(1)}+R_2^2L_2^{(-)}\hat{\Upsilon}_{32}^{(2)}\hat{\Upsilon}_{23}^{(2)}\right.\\
&\left.+R_3^2L_1^{(+)}\hat{\Upsilon}_{31}^{(3)}\hat{\Upsilon}_{13}^{(3)}+R_4^2L_2^{(+)}\hat{\Upsilon}_{32}^{(4)}\hat{\Upsilon}_{23}^{(4)}\right)\hat{\rho}_{33}^{(0)}\\
&+\hat{\rho}_{33}^{(0)}\left(R_1^2L_1^{(-)*}\hat{\Upsilon}_{31}^{(1)}\hat{\Upsilon}_{13}^{(1)}+R_2^2L_2^{(-)*}\hat{\Upsilon}_{32}^{(2)}\hat{\Upsilon}_{23}^{(2)}\right.\\
&\left.+R_3^2L_1^{(+)*}\hat{\Upsilon}_{31}^{(3)}\hat{\Upsilon}_{13}^{(3)}+R_4^2L_2^{(+)*}\hat{\Upsilon}_{32}^{(4)}\hat{\Upsilon}_{23}^{(4)}\right)\\
&-2\gamma_{eg}S_{11}^{(-)}\hat{\Upsilon}_{31}^{(1)}\hat{\rho}_{11}^{(0)}\hat{\Upsilon}_{13}^{(1)}-2\gamma_{eg}S_{31}^{(+)}\hat{\Upsilon}_{31}^{(3)}\hat{\rho}_{11}^{(0)}\hat{\Upsilon}_{13}^{(3)}\\
&-2\gamma_{eg}S_{22}^{(-)}\hat{\Upsilon}_{32}^{(2)}\hat{\rho}_{22}^{(0)}\hat{\Upsilon}_{23}^{(2)}-2\gamma_{eg}S_{42}^{(+)}\hat{\Upsilon}_{32}^{(4)}\hat{\rho}_{22}^{(0)}\hat{\Upsilon}_{23}^{(4)}\\
&-R_1R_2\left(L_1^{(-)}+L_2^{(-)*}\right)\hat{\Upsilon}_{31}^{(1)}\hat{\rho}_{12}^{(-)}\hat{\Upsilon}_{23}^{(2)}\\
&-R_1R_2\left(L_2^{(-)}+L_1^{(-)*}\right)\hat{\Upsilon}_{32}^{(2)}\hat{\rho}_{21}^{(+)}\hat{\Upsilon}_{13}^{(1)}\\
&-R_3R_4\left(L_2^{(+)}+L_1^{(+)*}\right)\hat{\Upsilon}_{32}^{(4)}\hat{\rho}_{21}^{(-)}\hat{\Upsilon}_{13}^{(3)}e^{i\phi_{12}}\\
&-R_3R_4\left(L_1^{(+)}+L_2^{(+)*}\right)\hat{\Upsilon}_{31}^{(3)}\hat{\rho}_{12}^{(+)}\hat{\Upsilon}_{23}^{(4)}e^{-i\phi_{12}}\\
&\qquad+i\left(g_e/g_2\right)\Omega\left[\hat{F}_3,\hat{\rho}_{33}^{(0)}\right]=0. \qquad \text{(A19)}
\end{aligned}$$

$$\begin{aligned}
&\left(\Gamma+\gamma+2ik_{12}\upsilon+R_1^2M_1^{(-)}\hat{\Upsilon}_{31}^{(1)}\hat{\Upsilon}_{13}^{(1)}\right.\\
&\left.+R_4^2M_2^{(+)}\hat{\Upsilon}_{32}^{(4)}\hat{\Upsilon}_{23}^{(4)}\right)\hat{\rho}_{33}^{(+)}+i(g_e/g_2)\Omega\left[\hat{F}_3,\hat{\rho}_{33}^{(+)}\right]\\
&+\hat{\rho}_{33}^{(+)}\left(R_2^2M_2^{(-)*}\hat{\Upsilon}_{32}^{(2)}\hat{\Upsilon}_{23}^{(2)}+R_3^2M_1^{(+)*}\hat{\Upsilon}_{31}^{(3)}\hat{\Upsilon}_{13}^{(3)}\right)\\
&-R_1^2M_1^{(-)}\hat{\Upsilon}_{31}^{(1)}\hat{\rho}_{11}^{(+)}\hat{\Upsilon}_{13}^{(1)}-R_3^2M_1^{(+)*}\hat{\Upsilon}_{31}^{(3)}\hat{\rho}_{11}^{(+)}\hat{\Upsilon}_{13}^{(3)}\\
&-R_2^2M_2^{(-)*}\hat{\Upsilon}_{32}^{(2)}\hat{\rho}_{22}^{(+)}\hat{\Upsilon}_{23}^{(2)}-R_4^2M_2^{(+)}\hat{\Upsilon}_{32}^{(4)}\hat{\rho}_{22}^{(+)}\hat{\Upsilon}_{23}^{(4)}\\
&-R_1R_2\left(M_1^{(-)}+M_2^{(-)*}\right)\hat{\Upsilon}_{31}^{(1)}\hat{\rho}_{12}^{(+)}\hat{\Upsilon}_{23}^{(2)}\\
&\quad-R_3R_4\left(M_1^{(+)*}+M_2^{(+)}\right)\hat{\Upsilon}_{32}^{(4)}\hat{\rho}_{21}^{(+)}\hat{\Upsilon}_{13}^{(3)}e^{i\phi_{12}}=0. \quad \text{(A20)}
\end{aligned}$$

The Hermitian conjugated equation (A20) gives the equation for $\hat{\rho}_{33}^{(-)}$.

For the low frequency coherences, we get:

$$\begin{aligned}
&\left(\Gamma+i\left[\delta_{\mathrm{R}}+k_{12}\upsilon\right]+R_1^2M_2^{(-)*}\hat{\Upsilon}_{13}^{(1)}\hat{\Upsilon}_{31}^{(1)}\right.\\
&\left.+R_3^2L_2^{(+)*}\hat{\Upsilon}_{13}^{(3)}\hat{\Upsilon}_{31}^{(3)}\right)\hat{\rho}_{12}^{(+)}-i\Omega\left(\hat{F}_1\hat{\rho}_{12}^{(+)}+\hat{\rho}_{12}^{(+)}\hat{F}_2\right)\\
&+\hat{\rho}_{12}^{(+)}\left(R_2^2M_1^{(-)}\hat{\Upsilon}_{23}^{(2)}\hat{\Upsilon}_{32}^{(2)}+R_4^2L_1^{(+)}\hat{\Upsilon}_{23}^{(4)}\hat{\Upsilon}_{32}^{(4)}\right)\\
&+R_1R_2M_1^{(-)}\hat{\rho}_{11}^{(+)}\hat{\Upsilon}_{13}^{(1)}\hat{\Upsilon}_{32}^{(2)}+R_3R_4L_1^{(+)}\hat{\rho}_{11}^{(0)}\hat{\Upsilon}_{13}^{(3)}\hat{\Upsilon}_{32}^{(4)}e^{i\phi_{12}}\\
&+R_1R_2M_2^{(-)*}\hat{\Upsilon}_{13}^{(1)}\hat{\Upsilon}_{32}^{(2)}\hat{\rho}_{22}^{(+)}+R_3R_4L_2^{(+)*}\hat{\Upsilon}_{13}^{(3)}\hat{\Upsilon}_{32}^{(4)}\hat{\rho}_{22}^{(0)}e^{i\phi_{12}}\\
&-R_1R_2\left(M_1^{(-)}+M_2^{(-)*}\right)\hat{\Upsilon}_{13}^{(1)}\hat{\rho}_{33}^{(+)}\hat{\Upsilon}_{32}^{(2)}\\
&\quad-R_3R_4\left(L_1^{(+)}+L_2^{(+)*}\right)\hat{\Upsilon}_{13}^{(3)}\hat{\rho}_{33}^{(0)}\hat{\Upsilon}_{32}^{(4)}e^{i\phi_{12}}=0. \qquad \text{(A21)}
\end{aligned}$$

$$\begin{aligned}
&\left(\Gamma+i\left[\delta_{\mathrm{R}}-k_{12}\upsilon\right]+R_1^2L_2^{(-)*}\hat{\Upsilon}_{13}^{(1)}\hat{\Upsilon}_{31}^{(1)}\right.\\
&\left.+R_3^2M_2^{(+)*}\hat{\Upsilon}_{13}^{(3)}\hat{\Upsilon}_{31}^{(3)}\right)\hat{\rho}_{12}^{(-)}-i\Omega\left(\hat{F}_1\hat{\rho}_{12}^{(-)}+\hat{\rho}_{12}^{(-)}\hat{F}_2\right)\\
&+\hat{\rho}_{12}^{(-)}\left(R_2^2L_1^{(-)}\hat{\Upsilon}_{23}^{(2)}\hat{\Upsilon}_{32}^{(2)}+R_4^2M_1^{(+)}\hat{\Upsilon}_{23}^{(4)}\hat{\Upsilon}_{32}^{(4)}\right)\\
&+R_1R_2L_1^{(-)}\hat{\rho}_{11}^{(0)}\hat{\Upsilon}_{13}^{(1)}\hat{\Upsilon}_{32}^{(2)}+R_3R_4M_1^{(+)}\hat{\rho}_{11}^{(-)}\hat{\Upsilon}_{13}^{(3)}\hat{\Upsilon}_{32}^{(4)}e^{i\phi_{12}}\\
&+R_1R_2L_2^{(-)*}\hat{\Upsilon}_{13}^{(1)}\hat{\Upsilon}_{32}^{(2)}\hat{\rho}_{22}^{(0)}+R_3R_4M_2^{(+)*}\hat{\Upsilon}_{13}^{(3)}\hat{\Upsilon}_{32}^{(4)}\hat{\rho}_{22}^{(-)}e^{i\phi_{12}}\\
&-R_1R_2\left(L_1^{(-)}+L_2^{(-)*}\right)\hat{\Upsilon}_{13}^{(1)}\hat{\rho}_{33}^{(0)}\hat{\Upsilon}_{32}^{(2)}\\
&\qquad-R_3R_4\left(M_1^{(+)}+M_2^{(+)*}\right)\hat{\Upsilon}_{13}^{(3)}\hat{\rho}_{33}^{(-)}\hat{\Upsilon}_{32}^{(4)}e^{i\phi_{12}}=0. \quad \text{(A22)}
\end{aligned}$$

Since $\hat{\rho}_{21}^{(-)}=\hat{\rho}_{12}^{(+)\dagger}$ and $\hat{\rho}_{21}^{(+)}=\hat{\rho}_{12}^{(-)\dagger}$, the other two equations can be obtained directly by Hermitian conjugation of the last two equations.

In (A15)–(A22), several new notations have been introduced. The saturation parameters are:

$$S_{n1}^{(\pm)}=R_n^2\left|L_1^{(\pm)}\right|^2 \qquad (n=1,3), \qquad \text{(A23)}$$

$$S_{n2}^{(\pm)}=R_n^2\left|L_2^{(\pm)}\right|^2 \qquad (n=2,4), \qquad \text{(A24)}$$

and the complex Lorentzians:

$$L_1^{(\pm)}=\left[\gamma_{eg}+i\left(\delta+\frac{\delta_{\mathrm{R}}}{2}\pm k_1\upsilon\right)\right]^{-1}, \qquad \text{(A25)}$$

$$L_2^{(\pm)}=\left[\gamma_{eg}+i\left(\delta-\frac{\delta_{\mathrm{R}}}{2}\pm k_2\upsilon\right)\right]^{-1}, \qquad \text{(A26)}$$

$$M_1^{(\pm)}=\left[\gamma_{eg}+i\left(\delta+\frac{\delta_{\mathrm{R}}}{2}\pm\left(2k_2-k_1\right)\upsilon\right)\right]^{-1}, \quad \text{(A27)}$$

$$M_2^{(\pm)}=\left[\gamma_{eg}+i\left(\delta-\frac{\delta_{\mathrm{R}}}{2}\pm\left(2k_1-k_2\right)\upsilon\right)\right]^{-1}. \quad \text{(A28)}$$

The excited-state population W_e can be obtained by numerically solving the equations (A15)–(A22).

REFERENCES

[1] S. Haroche and F. Hartmann, Phys. Rev. A **6**, 1280 (1972).

[2] C. Wieman and T. W. Hänsch, Phys. Rev. Lett. **36**, 1170 (1976).

[3] V. S. Letokhov and V. P. Chebotaev, “Nonlinear laser spectroscopy”, Springer, Berlin (1977).

[4] W. Demtröder, “Laser Spectroscopy: Basic concepts and instrumentation”, Third edition, Springer-Verlag, Berlin (2003).

[5] R.L. Barger and J.L. Hall, Phys. Rev. Lett. **22**, 4 (1969).

[6] T. W. Hänsch, M. D. Levenson, and A. L. Schawlow, Phys. Rev. Lett. **26**, 946 (1971).

[7] J. L. Hall, C. J. Bordé, and K. Uehara, Phys. Rev. Lett. **37**, 1339 (1976).

[8] A. M. Akulshin, V.L. Velichanskii, A.S. Zibrov, V.V. Nikitin, V.V. Sautenkov, E.K. Yurkin, and N.V. Senkov, JETP Lett. **36**, 303 (1982).

[9] G. D. Rovera, G. Santarelli and A. Clairon, Rev. Sci. Instr. **65**, 1502 (1998).

[10] C. Affolderbach and G. Mileti, Opt. Lasers Eng. **43**, 291 (2005).

[11] W. Liang, S. Ilchenko, D. Eliyahu, E. Dale, A.A. Savchenkov, D. Seidel, A. B. Matsko and L. Maleki, Appl. Opt. **54**, 3353 (2015).

[12] J. Ye, L. Robertsson, S. Picard, Long-Sheng Ma, and J.L. Hall, IEEE Trans. Instrum. Measur. **48**, 544 (1999).

[13] N. Chiodo, F. Du-Burck, J. Hrabina, M. Lours, E. Chea, and O. Acef, Opt. Lett. **39**, 2936 (2014).

[14] C. Philippe, D. Holleville, R. Le Targat, P. Wolf, T. Leveque, R. Le Goff, E. Martaud, and O. Acef, Proc. SPIE **10562**, 1056253 (2016).

[15] T. Schuldt, K. Döringshoff, E.V. Kovalchuk, A. Keetman, J. Pahl, A. Peters, and C. Braxmaier, Appl. Opt. **56**, 1101 (2017).

[16] M. Abdel Hafiz, G. Coget, E. De Clercq, and R. Boudot, Opt. Lett. **41**, 2982 (2016).

[17] P. Yun, F. Tricot, C. E. Calosso, S. Micalizio, B. Francois, R. Boudot, S. Guérandel, and E. de Clercq, Phys. Rev. Appl. **7**, 014018 (2017).

[18] M. Abdel Hafiz, G. Coget, P. Yun, S. Guérandel, E. de Clercq, and R. Boudot, J. Appl. Phys. **121**, 104903 (2017).

[19] M. Abdel Hafiz, D. Brazhnikov, A. Taichenachev, V. Yudin, E. de Clercq and R. Boudot, New J. Phys. **19**, 073028 (2017).

[20] G. Alzetta, A. Gozzini, L. Moi and G. Orriols, Nuovo Cimento B **36**, 5 (1976).

[21] V.S. Smirnov, A.M. Tumaikin and V.I. Yudin, Zh. Eksp. Teor. Fiz. **96**, 1613 (1989) [Sov. Phys. JETP **69**, 913 (1989)].

[22] E. Arimondo, Prog. Optics **35**, 257 (1996).

[23] R. Lutwak, A. Rashed, M. Varghese, G. Tepolt, J. LeBlanc, M. Mescher, D.K. Serkland, K.M. Geib, G.M. Peake, and S. Römisch, “The chip-scale atomic clock – Prototype evaluation”, 39th Precise Time and Time Interval Meeting (PTTI), pp. 269-290 (2007).

[24] R. Vicarini, V. Maurice, M. Abdel Hafiz, J. Rutkowski, C. Gorecki, N. Passilly, L. Ribetto, V. Gaff, V. Volant, S. Galliou and R. Boudot, Sensors Actuators A **280**, 99 (2018).

[25] Y. Zhang, W. Yang, S. Zhang and J. Zhao, J. Opt. Soc. Am. B **33**, 1756 (2016).

[26] https://www.microsemi.com/product-directory/clocks-frequency-references/3824-chip-scale-atomic-clock-csac

[27] W. Loh, M.T. Hummon, H.F. Leopardi, T.M. Fortier, F. Quinlan, J. Kitching, S.B. Papp, and S.A. Diddams, Opt. Exp. **24**, 14513 (2016).

[28] M. T. Hummon, S. Kang, D.G. Bopp, Q. Li, D.A. Westly, S. Kim, C. Fredrick, S.A. Diddams, K. Srinivasan, V. Aksyuk, and J.E. Kitching, Optica **5**, 443 (2018).

[29] Z. L. Newmann et al.,Arxiv 1811.00616 (2018).

[30] D.A. Varshalovich, A.N. Moskalev and V.K. Khersonskii, “Quantum Theory of Angular Momentum”, World Scientific, Singapore, 1988.

[31] J. Ishikawa, F. Riehle, J. Helmcke, and C.J. Bordé, Phys. Rev. A **49**, 4794 (1994).

[32] D.V. Brazhnikov and A.S. Novokreshchenov, Opt. Spectrosc. **122**, 541 (2017).

[33] D.B. Lazebnyi, D.V. Brazhnikov, A.V. Taichenachev, M.Yu. Basalaev, and V.I. Yudin, J. Exp. Theor. Phys. **121**, 934 (2015).

[34] D.V. Kosachiov, B.G. Matisov, and Yu.V. Rozhdestvensky, J. Phys. B **25**, 2473 (1992).

[35] C. Affolderbach, S. Knappe, R. Wynands, A.V. Taĭchenachev, and V.I. Yudin, Phys. Rev. A **65**, 043810 (2002).

[36] X. Liu, J.-M. Mérolla, S. Guérandel, C. Gorecki, E. de Clercq, and R. Boudot, Phys. Rev. A**87**, 013416 (2013).

[37] D.V. Brazhnikov, A.V. Taichenachev, A.M. Tumaikin, V.I. Yudin, I.I. Ryabtsev, and V.M. Entin, JETP Lett. **91**, 625 (2010).

[38] D.V. Brazhnikov, A.V. Taichenachev, and V.I. Yudin, Eur. Phys. J. D **63**, 315 (2011).

[39] A. Douahi, L. Nieradko, J. Beugnot, J. Dziuban, H. Maillote, S. Guerandel, M. Moraja, C. Gorecki, and V. Giordano, Electron. Lett. **43**, 4 (2007).

[40] M. Hasegawa, R.K. Chutani, C. Gorecki, R. Boudot, P. Dziuban, V. Giordano, S.Clatot, and L. Mauri, Sensor. Actuat A-Phys. **167**, 594 (2011).

[41] A.M. Akulshin, V.A. Sautenkov, V.L. Velichansky, A.S. Zibrov, and M.V. Zverkov, Opt. Commun. **77**, 295 (1990).

[42] V.V. Vasil'ev, V.L. Velichanskii, S.A. Zibrov, A.V. Sivak, D.V. Brazhnikov, A.V. Taichenachev, and V.I. Yudin, JETP **112**, 770 (2011).